Nonisothermal Crystallization Behavior of a Biodegradable Segmented Copolymer Constituted by Glycolide and Trimethylene Carbonate Units

Elena Díaz-Celorio, Lourdes Franco, Jordi Puiggalí

Departament d'Enginyeria Química, Universitat Politècnica de Catalunya, Av. Diagonal 647, E-08028, Barcelona, Spain

Received 3 November 2009; accepted 15 May 2010
DOI 10.1002/app.32816
Published online 19 August 2010 in Wiley Online Library (wileyonlinelibrary.com).

ABSTRACT: Nonisothermal crystallization of a segmented copolymer constituted by glycolide and trimethylene carbonate units was studied from both the melt and the glass state by optical microscopy, differential scanning calorimetry and time-resolved X-ray diffraction techniques. Positive spherulites with a fibrilar appearance were always obtained and corresponded to the crystallization of the polyglycolide hard segments. A single crystallization regime and the kinetic parameters were inferred from optical microscopy data on crystallizations performed at different cooling/heating rates. The parameters were in good agreement with values previously deduced from isothermal experiments. Isoconversional data of melt and glass nonisothermal crystallizations were combined to obtain the Lauritzen and Hoffman parameters from calorimetric data. Results revealed again the existence of a single crystallization regime with a secondary nucleation constant close to that deduced from isothermal DSC experiments. Morphological changes occurring during the hot and cold crystallization were evaluated by time-resolved SAXS/WAXD experiments employing synchrotron radiation. Measurements showed that significant differences on the lamellar thicknesses exist depending on the crystallization process.
 J Appl Polym Sci 119: 1548–1559, 2011

Key words: polyglycolide; surgical sutures; nonisothermal crystallization; differential scanning calorimetry; isoconversional methods; synchrotron radiation

INTRODUCTION

Glycolide (GL) and its copolymers with different lactones and/or cyclic carbonates are widely used in the biomedical field due to their biodegradability, biocompatibility, and physical properties, which meet the requirements of specific applications.[1–8]

Maxon™ (Syneture) is probably the most simple bioabsorbable monofilament suture derived from GL nowadays commercialized.[9,10] This copolymer incorporates trimethylene carbonate (TMC) units which provide elastomeric characteristics that compensate for the high stiffness of polyglycolide. In fact, the sample has a segmented nature because of the two-step synthesis procedure (Scheme 1). First, a middle soft segment with a theoretically random distribution of the two-monomer units is prepared by copolymerization of GL and TMC; second, hard segments derived from GL units are incorporated at both ends of the polymer chain. The GL content is close to a molar percentage of 63%, whereas this percentage decreases up to 12% in the middle soft segment. This copolymer will therefore be called PGL-P(GL-*co*-TMC)-PGL to emphasize its segmented nature.

It has been proved that the hard and soft segments of this copolymer are completely miscible and that only the polyglycolide blocks are involved in the crystallization process.[11] This is very significant as the crystallinity of the sample influences both the mechanical properties and degradability, which are determining features in uses such as bioabsorbable sutures. Furthermore, comprehension of the crystallization process in a polymer system where amorphous and crystalline domains coexist is an interesting topic.

Thus, an accurate isothermal crystallization study of PGL-P(GL-*co*-TMC)-PGL was recently conducted.[11] It was determined that crystallization is characterized by a low primary nucleation density and a secondary nucleation constant close to 1.82–1.86 $\times$ 10^5 K^2. Interestingly, the isothermal studies indicated that nucleation was athermal (i.e., the number of nuclei remained constant during crystallization) and that the plot of the overall crystallization rate versus the crystallization temperature matched that of the crystal growth rate.

Correspondence to: J. Puiggalí (Jordi.Puiggali@upc.es).
Contract grant sponsor: FEDER; contract grant numbers: MAT 2006-02406, MAT2009-11503.
Contract grant sponsor: CICYT.

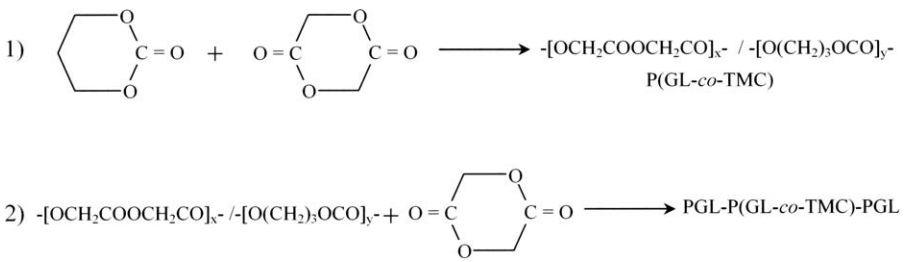

Scheme 1 Two-step synthesis of the segmented copolymer.

The present work studies nonisothermal crystallization of PGL-P(GL-*co*-TMC)-PGL given that processing for industrial applications may sometimes occur at a variable temperature. Moreover, the low crystallization rate and athermal nucleation make this polymer particularly suitable for evaluation of recently developed methods for deriving crystallization data from faster nonisothermal experiments. These were conducted either from the glass and the melt state and analyzed by both calorimetric and optical microscopy techniques. Control of both crystallinity and polymer morphology is a crucial point since final properties and even degradation rate are influenced by them. A final goal of this work corresponds to the study by synchrotron analysis of morphological changes that occurred during cold and hot nonisothermal crystallizations and even during thermal treatments from the glass state.

EXPERIMENTAL

Materials

Commercially available sutures of PGL-P(GL-*co*-TMC)-PGL (Maxon^{TM}) were purchased from Tyco Healthcare. Weight average molecular weight was 95,000 as determined by GPC from 1,1,1,3,3,3-hexafluroisopropanol solutions and using poly(methyl methacrylate) standards.

Measurements

Calorimetric data were obtained by differential scanning calorimetry with a TA Instruments Q100 series with T_{zero} technology and equipped with a refrigerated cooling system (RCS) operating at temperatures from -90°C to 550°C. Experiments were conducted under a flow of dry nitrogen with a sample weight of $\sim$ 5 mg and calibration was performed with indium. T_{zero} calibration requested two experiments: the first was done without samples and the second was performed with sapphire disks.

The spherulitic growth rate was determined by optical microscopy using a Zeiss Axioskop 40 Pol light polarizing microscope equipped with a Linkam temperature control system configured by a THMS 600 heating and freezing stage connected to a LNP 94 liquid nitrogen cooling system. Spherulites were grown from homogeneous melt-crystallized thin films obtained by melting 1 mg of the polymer over microscope slides. Next, small sections of these films were pressed or smeared between two cover slides and inserted into the hot stage. The thickness of the squeezed samples was in all cases close to 10 μm. Samples were kept at 215°C ($\sim$ 10°C above the polymer melting point of 202°C) for 5 min to wipe sample history effects. For hot crystallization experiments, the samples were rapidly cooled to a selected temperature (lower than the melting temperature), isothermally maintained during 3 minutes at this temperature for equilibration and then cooled at different rates (3 and 0.5°C/min) to increase the experimental crystallization temperature range (Scheme 2). It was stated that spherulites were not formed at the end of the second isothermal step according to optical microscopy observations. For cold crystallization experiments, the above melted samples were quenched in liquid nitrogen and then heated at rates of 1 and 0.5°C/min. The radius of the growing spherulites was monitored during crystallization with micrographs taken with a Zeiss AxiosCam MRC5 digital camera at appropriate time intervals.

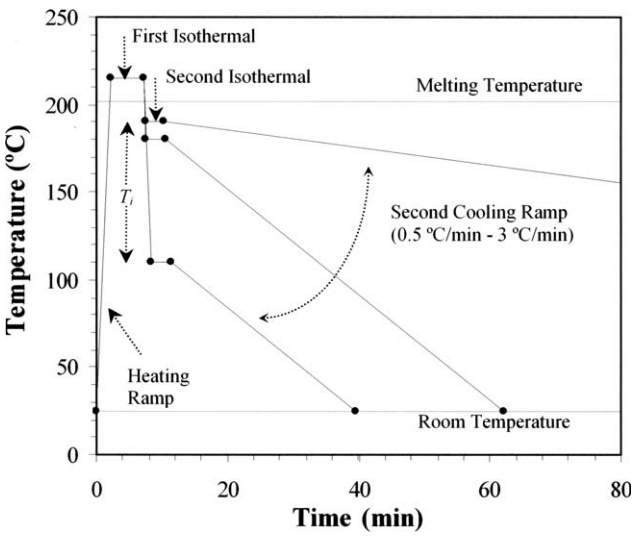

Scheme 2 Thermal program for optical microscopy hot crystallization experiments.

A first-order red tint plate was employed to determine the sign of spherulite birefringence under crossed polarizers.

Simultaneous time-resolved SAXS/WAXD experiments were carried out at the CRG beamline (BM16) of the European synchrotron radiation facility of Grenoble. The beam was monochromatized to a wavelength of 0.098 nm. The capillary with the sample was held in a Linkam hot stage with temperature control within 0.1°C. SAXS and WAXD profiles were acquired simultaneously during isothermal and cooling experiments in time frames of 12 s. Two linear position-sensitive detectors were used[12]: the SAXS detector was calibrated with different orders of diffraction from silver behenate whereas the WAXD detector was calibrated with diffractions of a standard of an alumina (Al_2O_3) sample. The diffraction profiles were normalized to the beam intensity and corrected considering the empty sample background. WAXD peaks were deconvoluted with the PeakFit v4 program by Jandel Scientific Software using a mathematical function known as "Gaussian and Lorentzian area" (Pearson VII function). The correlation function and corresponding parameters were calculated with the CORFUNC program[13] for Fiber Diffraction/Noncrystalline Diffraction, CCP13, provided by the Collaborative Computational Project 13.

RESULTS AND DISCUSSION

Nonisothermal study of the spherulitic growth rate of PGL-P(GL-*co*-TMC)-PGL

Nonisothermal procedures can be applied to study the temperature dependence of the spherulitic growth rate during cold and hot crystallization.[14–16] Thus, the spherulitic growth rate (G) can be estimated by measuring the change of the spherulite radius (R) with temperature (T) when experiments are performed at a constant cooling/heating rate (dT/dt):

$$G = dR/dt = (dR/dT)(dT/dt) \quad (1)$$

The plot of the radius versus temperature can be fitted to a polynomial equation with a good regression coefficient (r) that allows the calculation of the value of its first derivative (dR/dT) for each cooling/heating rate as a function of the crystallization temperature. Experimental problems lie in the choice of the cooling/heating rate required to maximize the crystallization temperature range where radii can be well measured. For this reason, the use of various rates is highly effective in expanding this range.

Previous isothermal studies on PGL-P(GL-*co*-TMC)-PGL[11] indicate that spherulites with a fibrilar texture, positive birefringence, and measurable growth rate form in the temperature ranges of 75–97°C and 160–186°C for cold and hot crystallizations, respectively. These values indicate the crystallization range that should be covered by the nonisothermal experiments. All hot crystallizations were performed in two steps to avoid problems associated with the long induction time required for nuclei to be active. Thus, samples were first kept at a selected temperature, T_i, and then cooled at a certain rate. Experimental measurements could be extended to a wide temperature range by choosing different T_i temperatures. Note that the nucleation density of the studied thin films was very low at the hot crystallization temperatures and that the spherulitic growth rate was moderate. That is why the crystallization process took a long time, and therefore a large temperature interval could be covered in these hot crystallization experiments. On the contrary, the nucleation density was higher at the initial temperatures required for the cold crystallizations experiments. In this case, variation of the heating rate was the only way to increase the temperature interval to obtain cold crystallization experimental data.

Spherulites obtained at the end of cold and hot nonisothermal crystallizations performed at a representative cooling/heating rate are shown in Figure 1. The fibrilar and positive spherulites observed in a determined cold crystallization experiment have a similar size, whereas greater variability was detected in the few spherulites that formed in the hot crystallized sample. In this case, nuclei became progressively active during the cooling rate, the smaller spherulites corresponding to those that appeared at lower crystallization temperatures. A positive birefringence and a fibrilar texture were again detected.

The change in the radius of a typical spherulite of PGL-P(GL-*co*-TMC)-PGL during the temperature ramp at different cooling/heating rates is illustrated in Figure 2(a). In all crystallizations, a polynomial fitting with a high regression coefficient was obtained. Third-order equations were always chosen (Table I) since the regression coefficients ($\geq$ 0.998) were slightly better than those calculated for lower-order equations and remained constant when higher orders were assayed.

The relationships between the spherulitic growth rate and crystallization temperature were obtained by differentiating the above third-order equations with respect to the temperature and considering the cooling/heating rate [eq. (1)]. Figure 2(b) plots the G values deduced for different cooling/heating rates and T_i temperatures as a function of temperature. A bell-shaped curve with a maximum at 125°C was obtained. Note that experimental data practically cover all temperatures at which the crystallization rate is different from zero, a feature that was not possible when isothermal experiments were performed.[11] Note also that growth rates could be measured in the

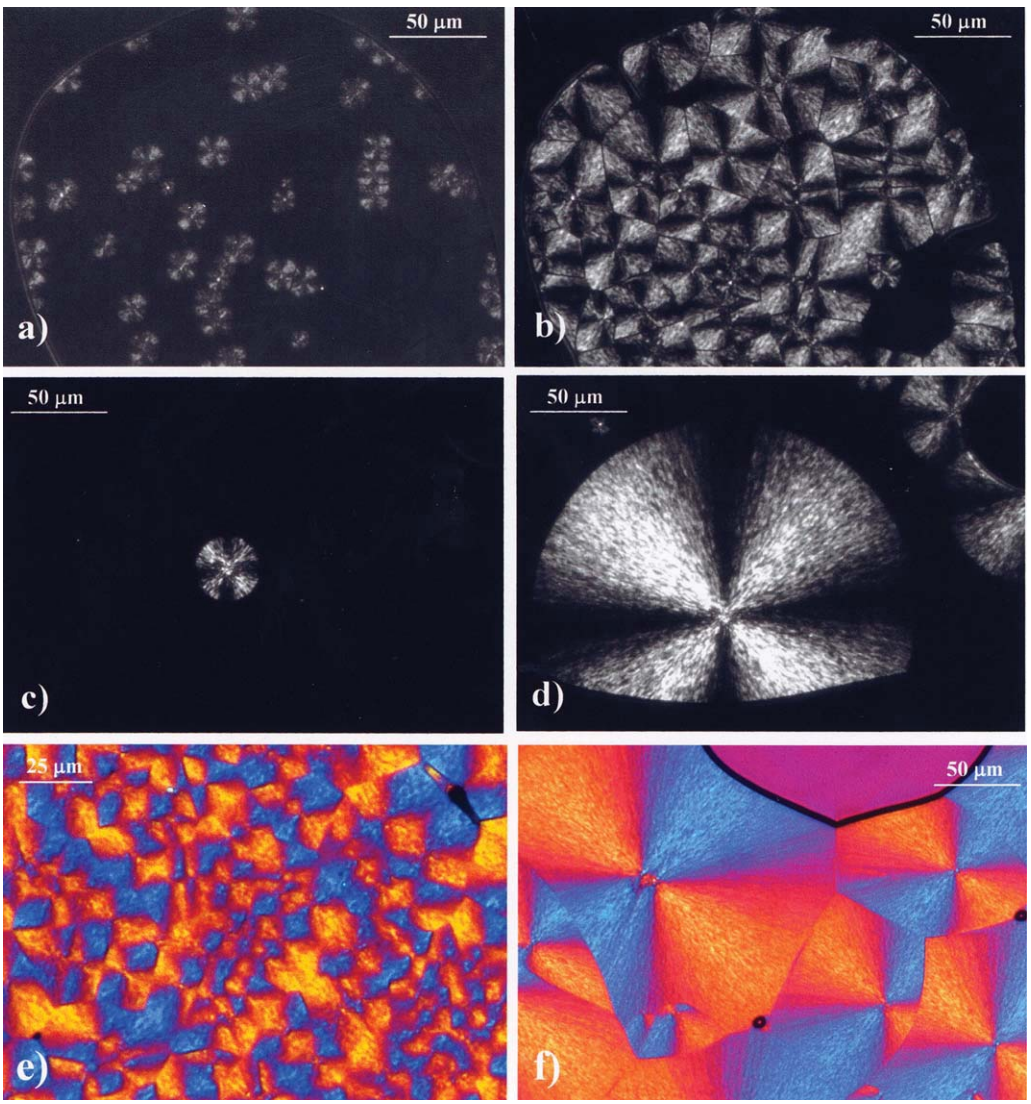

Figure 1 Polarized optical micrographs showing spherulites of cold (a, b) and hot (c, d) nonisothermally crystallized samples of PGL-P(GL-*co*-TMC)-PGL obtained at a heating/cooling rate of 0.5°C/min. Micrographs correspond to the earlier (a,c) and later (b, d) stages of crystallization. Hot crystallization was performed from an initial temperature of 190°C. Micrographs taken at the end of crystallization using a first-order tint plate revealed a positive birefringence for both cold (e) and hot (f) crystallized samples. [Color figure can be viewed in the online issue, which is available at wileyonlinelibrary.com.]

low temperature range (57–85°C) by considering either cold or hot crystallization experiments. A good agreement was found between data obtained from these two different crystallization procedures.

Crystallization regimes were analyzed by considering the values of the radial growth rate (G) deduced from the nonisothermal experiments and using the well known Lauritzen and Hoffman equation[17]:

$$G = G_0 \exp\left[-\frac{U^*}{R(T_c - T_\infty)}\right] \exp\left[-\frac{K_g}{T_c(\Delta T)f}\right] \quad (2)$$

where G_0 is a constant pre-exponential factor, U^* denotes the activation energy characteristic of the transport of crystallizing segments across the liquid-crystal interface, T_∞ is a hypothetical temperature below which such motion ceases, T_c is the crystallization temperature, T_m^0 is the equilibrium melting point, R is the gas constant, K_g is the nucleation parameter, ΔT is the degree of supercooling measured as $T_m^0 - T_c$, and f is a correction factor accounting for the variation in the bulk melting enthalpy per unit volume with temperature ($f = 2T_c/(T_m^0 + T_c)$).

The glass transition temperature and equilibrium melting point had values of 20 and 225°C, respectively, as previously determined.[11]

Figure 2(c) shows the characteristic Lauritzen and Hoffman plot obtained from the nonisothermal growth data. A linear fit was found with U^* and T_∞

parameters of 1575 cal/mol and T_g – 30 K, respectively, which are very close to the conventional parameters reported by Suzuki and Kovacs[18] (U^* = 1500 cal/mol and $T_\infty = T_g - 30$ K). The slope of the Lauritzen and Hoffman plot indicated that the single crystallization regime was defined by a secondary nucleation constant of 2.45 10^5 K^2 which is in close agreement with the value previously found from isothermal analysis[11] (1.82 10^5 K^2).

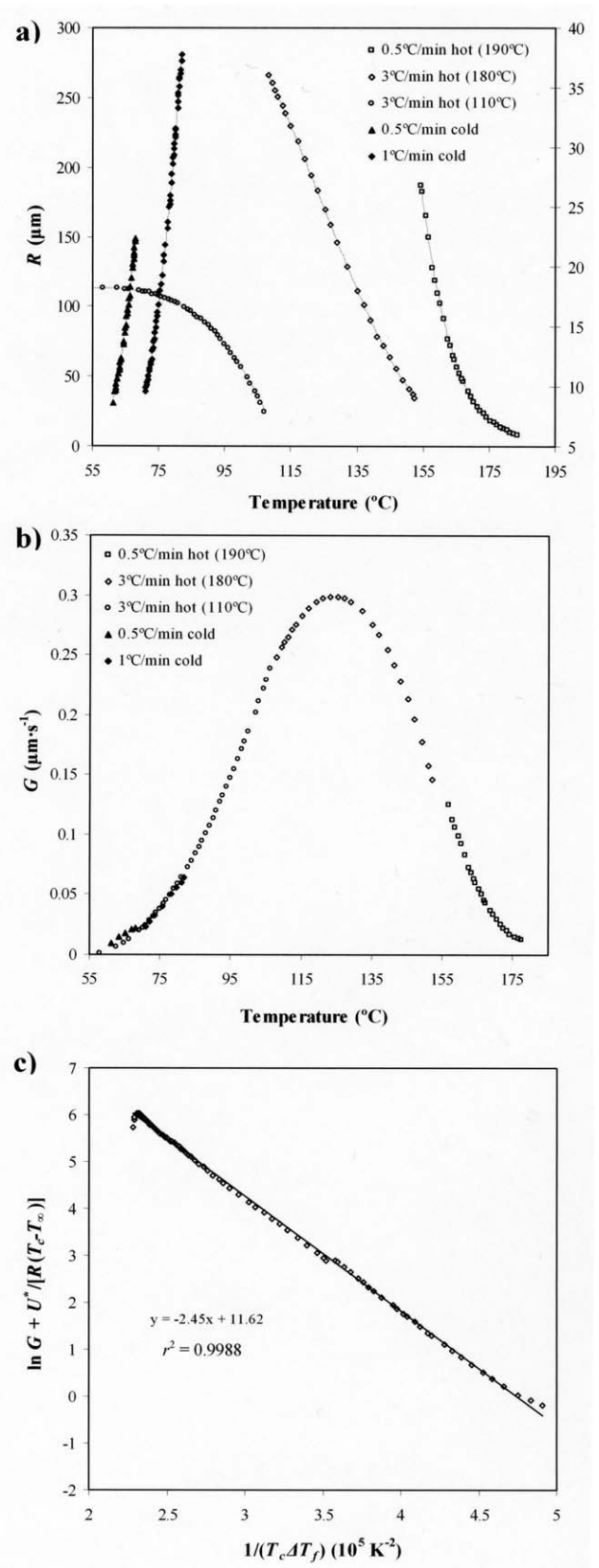

Figure 2 a) Variation in spherulite radius with temperature during heating (full symbols and right ordinate scale) and cooling (empty symbols and left ordinate scale) at the indicated rates and starting crystallization temperatures. (b) Spherulitic growth rates determined by the equations deduced for cooling (empty symbols) and heating (full symbols) runs. (c) Kinetic analysis of growth rate data for PGL-P(GL-*co*-TMC)-PGL by eq. (2) and parameters U* = 1575 cal/mol, $T_\infty = T_g$ – 30 K and K_g = 2.45 10^5 K^2.

Nonisothermal DSC crystallization study of PGL-P(GL-*co*-TMC)-PGL

Figure 3 (insets) shows dynamic DSC curves obtained from quenched and melted samples at different heating and cooling rates, respectively. Crystallization peaks become sharper and their temperature progressively shifts to higher and lower values when the heating and the cooling rates are respectively increased. Cold crystallization peaks are characterized by an asymmetric shape with a long tail, suggesting a complex crystallization process. In fact, previous isothermal crystallization studies[11] indicate that a subsequent crystallization occurred at temperatures slightly higher than those corresponding to the main crystallization. On the contrary, hot crystallization peaks are narrow and symmetric.

The relative degree of crystallinity at any temperature, $\chi(T)$, and for each cooling/heating rate was determined with calorimetric data by the expression:

$$\chi(T) = \frac{\int_{T_0}^{T_c} (dH_c/dT)dT}{\int_{T_0}^{T_\infty} (dH_c/dT)dT} \quad (3)$$

where dH_c is the enthalpy of crystallization released during an infinitesimal temperature range dT, T_0 denotes the initial crystallization temperature and T_c and T_∞ are the crystallization temperature at time t and after completion of the crystallization process, respectively. Thus, the denominator corresponds to the overall enthalpy of crystallization for specific heating/cooling conditions.

The relative degree of crystallinity can be calculated as a function of time by the relationship:

$$(t - t_0) = (T_0 - T)/\phi = (T - T_0)/\beta \quad (4)$$

where T_0 is the temperature at which crystallization begins ($t = t_0$) and ϕ and β are the values of the cooling and heating rates, respectively.

TABLE I
Third Order Equations that Fit the Temperature Dependence of PGL-P(GL-*co*-TMC)-PGL Spherulitic Radius During Hot and Cold Nonisothermal Crystallizations

Cooling rate (°C/min)	Hot crystallization Equation	r^2	Heating rate (°C/min)	Cold crystallization Equation	r^2
0.5[a]	$R = -0.00864\,T^3 + 4.6523\,T^2 - 836.7747\,T + 50261.936$	0.9997	0.5	$R = -0.00322\,T^3 + 0.73878\,T^2 - 53.1206\,T + 1230.836$	0.9984
3[b]	$R = 0.00132\,T^3 - 0.4902\,T^2 + 54.8728\,T - 1599.845$	0.9999	1	$R = 0.00036\,T^3 + 0.03136\,T^2 - 8.4413\,T + 323.4108$	0.9997
3[c]	$R = -0.00059\,T^3 + 0.0964\,T^2 - 5.2156\,T + 207.024$	0.9998			

[a] Starting crystallization temperature 190°C.
[b] Starting crystallization temperature 180°C.
[c] Starting crystallization temperature 110°C.

Figure 3 also illustrates the variation of the time-dependent degree of crystallinity, $\chi(t)$, at different cooling/heating rates. This data allow performing a kinetic analysis of hot/cold nonisothermal crystallization processes.

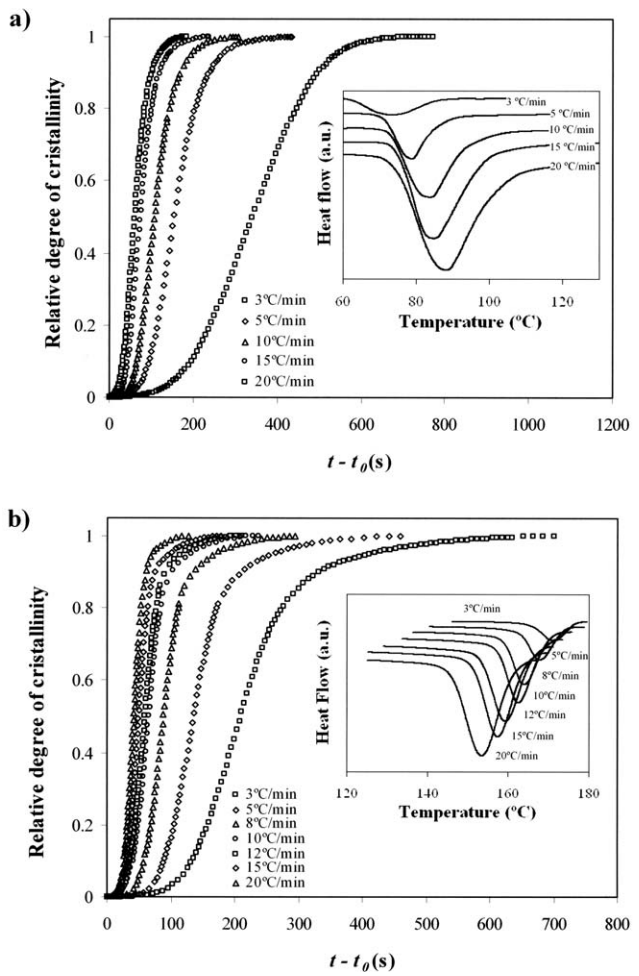

Figure 3 Time evolution of relative crystallinity at the indicated heating/cooling rates for the cold (a) and hot (b) crystallization of PGL-P(GL-*co*-TMC)-PGL. Insets show the corresponding dynamic DSC curves obtained at the indicated heating/cooling rates.

The kinetics of these crystallizations have a non-Arrheniusian behavior since two exponential functions are implied in the classical Lauritzen and Hoffman equation.[17] In this way, a temperature-dependent effective activation energy of the growth rate was defined and derived from this equation by Vyazovkin and Sbirrazzuoli[19]:

$$E(T) = -R\,\mathrm{d}\,\ln\,G/\mathrm{d}T^{-1} = U^*[T^2/(T-T_\infty)^2] + K_g R[(2\Delta T - T_m^0 f)/(\Delta T)^2 f] \quad (5)$$

A new methodology based on isoconversional analysis was developed to estimate the indicated temperature-dependent effective activation energies and successfully applied to evaluate the typical crystallization parameters from melt crystallization[19–25] and combined melt and glass crystallizations.[20,26] Note that this new approach can use nonisothermal calorimetric data instead of optical microscopy measures, which may be highly time consuming experiments, especially when are performed under isothermal conditions.

The isoconversional method of Friedman[27] considers a variation of the effective activation energy with crystallinity that follows the equation:

$$[d_\chi/d\,t]_\chi = A\,\exp\,(-E_\chi/RT) f[\chi] \quad (6)$$

where A is a preexponential factor and $f\,[\chi]$ is the crystallization model. Values of $\ln\,[d\chi/\mathrm{d}t]_\chi$ at different temperatures and conversion degrees can be obtained from the above indicated crystallization experiments performed at different heating/cooling rates. In this way, it is possible to determine E_χ from the slopes of the linear plots of $\ln\,[d\chi\ /dt]_\chi$ versus $1/T$ for hot and cold crystallization processes. The temperature dependence of the effective activation energy was finally derived by considering also the average temperature associated with a given conversion.

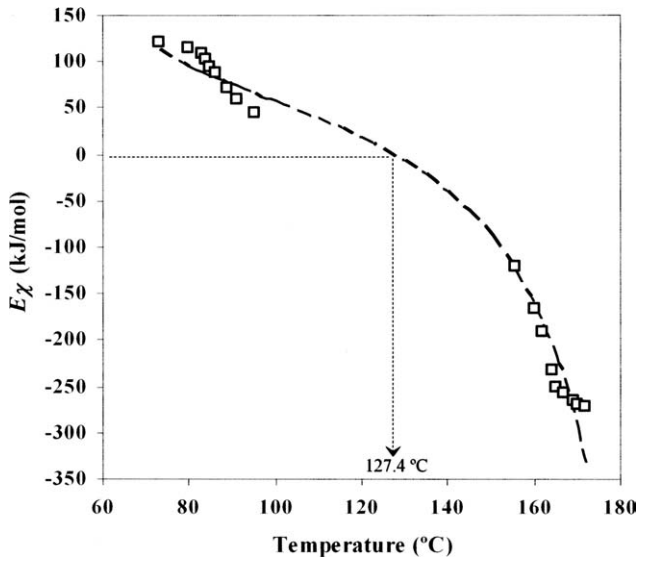

Figure 4 Experimental E_χ on T data for hot and nonisothermal cold crystallization of PGL-P(GL-*co*-TMC)-PGL. Dashed line corresponds to the data calculated by eq. (5) and the optimized crystallization parameters. Arrow indicates the expected temperature for the maximum crystallization rate (i.e., effective activation energy equal to zero).

Figure 4 displays the deduced $E_\chi - T$ plot for the hot and cold crystallization experiments. Effective activation energy data were fit to eq. (5) to evaluate the main kinetic parameters. The secondary nucleation constant was mainly deduced from the hot crystallization data since the other parameters have little influence on the temperature range, which is far from the glass transition temperature. On the contrary, the activation energy of the transport process, U^*, and the temperature, T_∞, were mainly determined from the cold crystallization data.

The best fit between experimental and theoretical data was obtained with U^*, T_∞ and K_g parameters of 1675 cal/mol, $T_g - 30$ K and 2.30×10^5 K^2, respectively. These values are fully consistent with those deduced from the above explained optical microscopy experiments. It is also interesting to note that previous isothermal crystallization studies[11] on PGL-P(GL-*co*-TMC)-PGL samples indicated a great agreement between the bell shaped curves that describe the temperature dependence of the overall crystallization rate and the crystal growth rate, a feature that suggests a linear dependence between the two indicated rates for the studied polymer.

The simulated $E_\chi - T$ plot (dashed line in Fig. 5) shows that the effective activation energy always increased with decreasing the crystallization temperature. This energy was negative at high crystallization temperatures (i.e., the zone controlled by secondary nucleation) and progressively increased with decreasing the temperature. The energy became zero at the maximum crystallization rate temperature and positive at lower temperatures (i.e., the zone controlled by the transport energy term). Negative and positive signs only indicate that the crystallization rate increased with decreasing and increasing temperatures, respectively, as discussed at length by Vyazovkin and Dranca.[20] The plot shows that the maximum crystallization rate is expected for a temperature of 127.4°C, which is in agreement with the value deduced from the isothermal study (130°C).[11]

Study on the nonisothermal crystallization of PGL-P(GL-*co*-TMC)-PGL by time-resolved SAXS/WAXD experiments

Figure 5 shows representative time-resolved SAXS and WAXD profiles of PGL-P(GL-*co*-TMC)-PGL obtained during a nonisothermal hot crystallization performed at 5°C/min. A SAXS long period peak is clearly seen at a value of the scattering vector, $q = [4\pi/\lambda] \sin(\theta)$, close to 0.045 Å^{-1} after subtraction of the empty sample background observed near the beam stop. This peak can be attributed to the lamellar structure of the spherulites and starts to appear at a temperature value which decreases with increasing the crystallization cooling rate. Subsequently, the peak intensity increases significantly with decreasing temperature until reaching a plateau value. For each cooling rate, the peak slightly shifts to higher q values during crystallization, the change being more pronounced in the initial stages. The high intensity of the final SAXS peaks, indicating a large difference between the electronic density of the amorphous and the crystalline phases, is worth pointing out. In fact, the crystalline structure of polyglycolide[28] is characterized by a very tight packing, as opposed to the less dense structures found in related aliphatic polyesters (e.g., poly-β-propiolactone[29]).

The initial WAXD profiles show two amorphous halos [inset of Fig. 5(b)] whose intensity decreases when crystallization occurs and on which Bragg reflections form. Those most intense appear at 0.400 nm ($q = 15.7$ nm^{-1}) and 0.310 nm ($q = 20.3$ nm^{-1}) and can be indexed as the (110) (020) reflections of the polyglycolide structure, defined by an orthorhombic unit cell having $a = 0.522$ nm, $b = 0.619$ nm, and $c = 0.702$ nm.[28] The intensities of these reflections increase significantly at the beginning of crystallization until reaching their maximum values after a short time interval. For a given cooling rate, the SAXS long period peak and crystal diffractions appear simultaneously, as expected for a crystallization process controlled by nucleation and crystal growth.

Similar trends were observed in the cold crystallization experiments performed at different heating rates. In this case, the scattering vector appeared at slightly higher values than those observed in the hot crystallization experiments performed at a similar

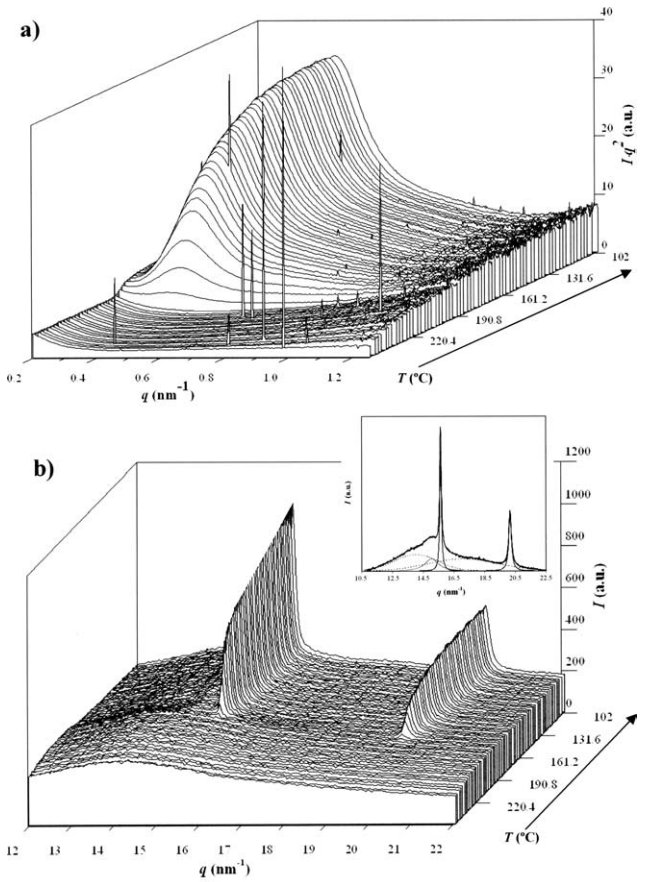

Figure 5 Time-resolved SAXS (a) and WAXD (b) three-dimensional profiles of PGL-P(GL-*co*-TMC)-PGL during nonisothermal hot crystallization at 5°C/min. SAXS curves are shown after subtraction of empty sample background and Lorentz correction. Inset of (b) shows the deconvolution of the WAXD profile at the end of nonisothermal crystallization.

rate (heating instead of cooling). SAXS profiles [Fig. 6(a)] showed also a continuous increase of the peak intensity after reaching the temperature at which cold crystallization could be considered finished according to the exothermic peak observed in the DSC thermogramas. This increase suggests a decrease of the electronic density of the interlamellar amorphous phase with increasing temperatures. The increase of the peak intensity was especially noticeable at some degrees before fusion. On the contrary, WAXD profiles [Fig. 6(b)] showed that crystalline reflections had a practically constant intensity after reaching the temperature at which cold crystallization could be considered finished. Thus, a significant increase on the degree of crystallinity could not be detected at high temperatures.

SAXS data were analyzed considering the normalized one-dimensional correlation function,[30] $\gamma(r)$, which corresponds to the Fourier transform of the Lorentz-corrected SAXS profile:

$$\gamma(r) = \int_0^\infty q^2 I(q) \cos(qr) dq \Big/ \int_0^\infty q^2 I(q) dq \qquad (7)$$

SAXS data were collected within a limited angular range only. That is why extrapolations to low and high q values were performed using Vonk's model[31] and Porod's law, respectively.

Figure 7(b) illustrates the correlation functions calculated for the SAXS profiles [Fig. 7(a)] obtained at the end of the nonisothermal experiments conducted at different cooling rates (i.e., at temperatures at which crystallization was ended according to DSC thermograms), whereas Figure 8 compares the correlation functions at the end of the hot and cold crystallizations performed at the lowest rate (3°C/min). The analysis of these functions generally allows the determination of: (1) the long period, L_γ, (i.e., the r value of the first maximum of the correlation function); (2) the amorphous layer thickness, l_a, (i.e., the r value for the intersection of the linear regression in the autocorrelation triangle with the ordinate equal to the first minimum of the correlation function); (3) the crystalline lamellar thickness, l_c, (calculated as L_γ((la); (4) the crystallinity within the lamellar stacks,

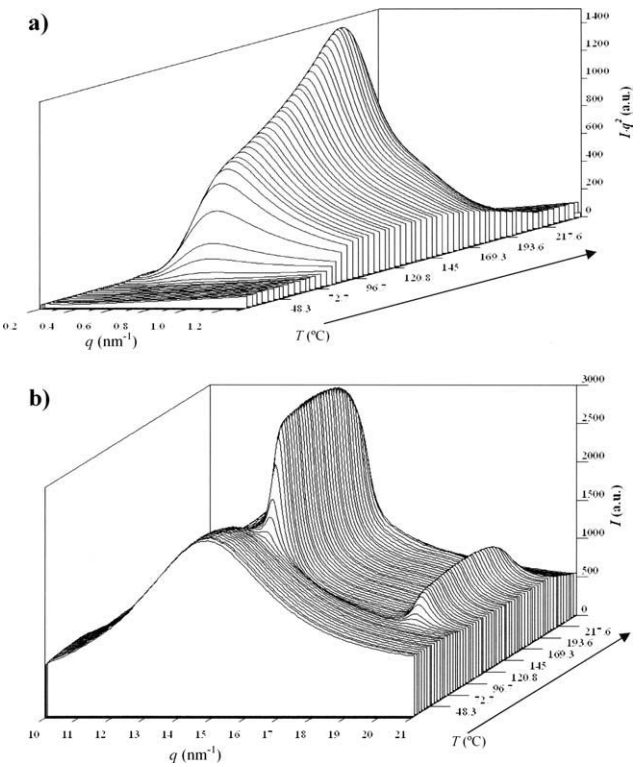

Figure 6 Time resolved SAXS (a) and WAXD (b) three-dimensional profiles of PGL-P(GL-*co*-TMC)-PGL during cold nonisothermal crystallization at 3°C/min. SAXS curves are shown after subtraction of empty sample background and Lorentz correction.

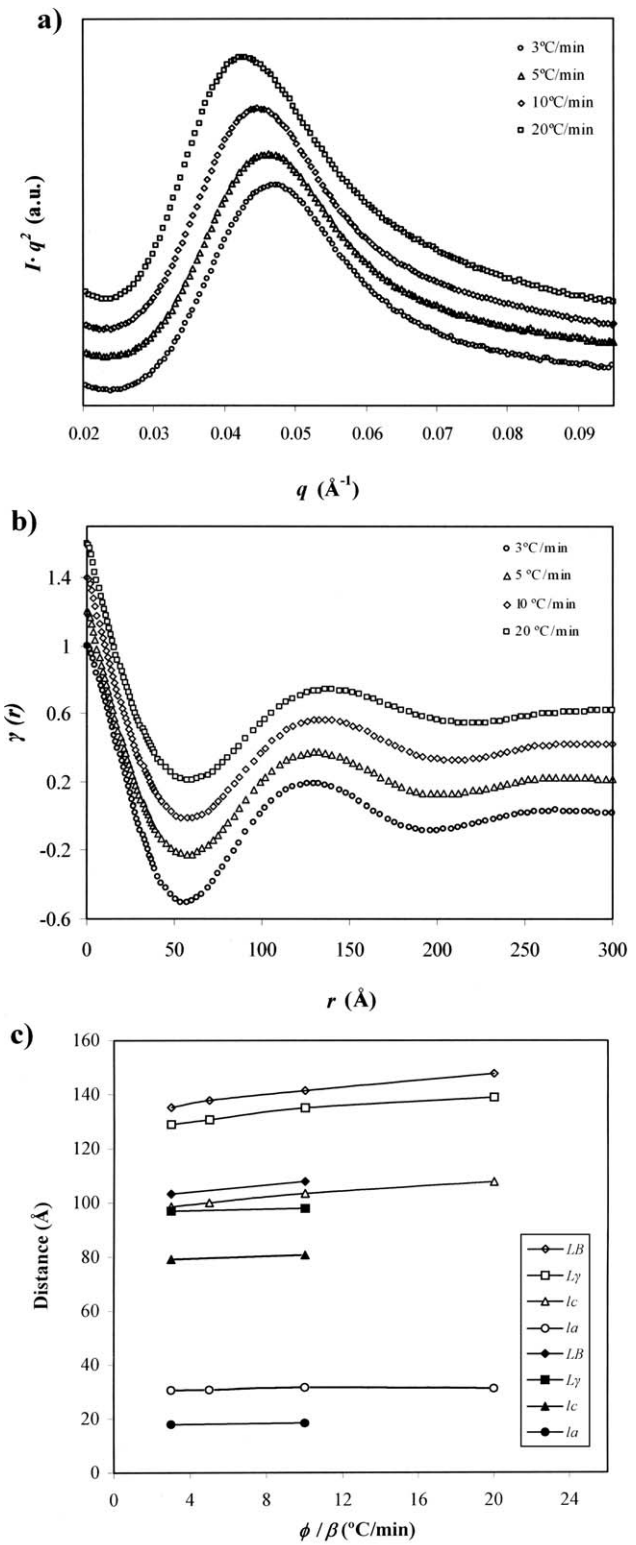

Figure 7 Final SAXS profiles (a) and corresponding correlation functions (b) at different cooling rates for nonisothermal hot crystallization of PGL-P(GL-*co*-TMC)-PGL. (c) L_B, $L_{\ddot{y}\,\ddot{\imath}}$, l_c, and l_a values obtained at the end of nonisothermal cold (full symbols) and hot (empty symbols) crystallization performed at different heating/cooling rates.

X_c^{SAXS} (calculated as l_c/L_γ; and (5) the scattering invariant, Q.

The long period deduced from the peak observed in the SAXS profiles (L_B) or from the correlation function (L_γ) clearly increases with the cooling rate [i.e., from 13.5–14.8 to 12.9–13.9 nm for rates between 3 and 20°C/min, as can be seen in Fig. 7(c)]. Increasing rates conduced to an increase (from 9.9–10.8 nm) of the crystalline lamellar thickness whereas the amorphous layer was not significantly affected. Interestingly, both crystalline and amorphous thicknesses remained practically constant in the cold crystallization experiments [Fig. 7(c)]. Comparison between cold and hot crystallization at a given rate (Fig. 8) clearly demonstrates that lamellae were thinner when spherulites were obtained from the glass state, that is, from lower crystallization temperatures (e.g., 9.7 and 12.9 nm were measured for samples crystallized at 3°C/min). Figure 8 shows also the correlation function of a cold crystallized sample just at some degrees) (20°C) before fusion. In this case, it is clear that the crystalline lamellar thickness increased significantly during the later heating step, whereas the amorphous thickness remained practically constant. This behavior clearly suggests that a melt-recrystallization process of the initial lamellae took place before melting.

The L_γ values were in all cases higher than the long period determined from twice the value of the first minimum of the correlation function (e.g., 12.9 nm and 11.4 nm for the crystallization performed at 3°C/min). Thus, the most probable distance between

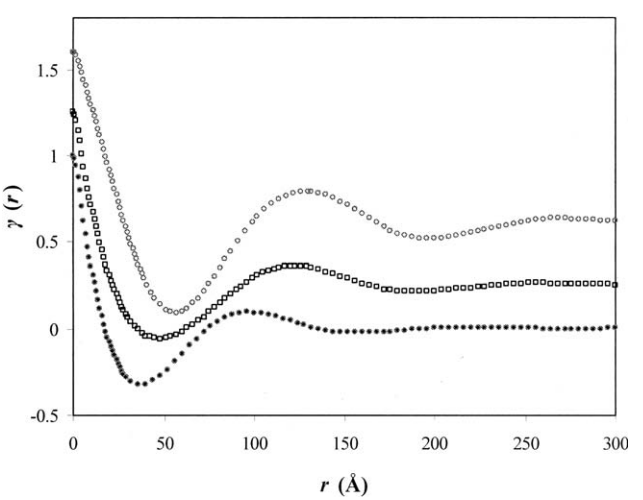

Figure 8 Comparison between correlation functions for cold (●) and hot (○) crystallized samples of PGL-P(GL-*co*-TMC)-PGL at a heating/cooling rate of 3°C/min. The correlation function of a heated sample (3°C/min) after completing both cold and hot recrystallization processes is also shown (□).

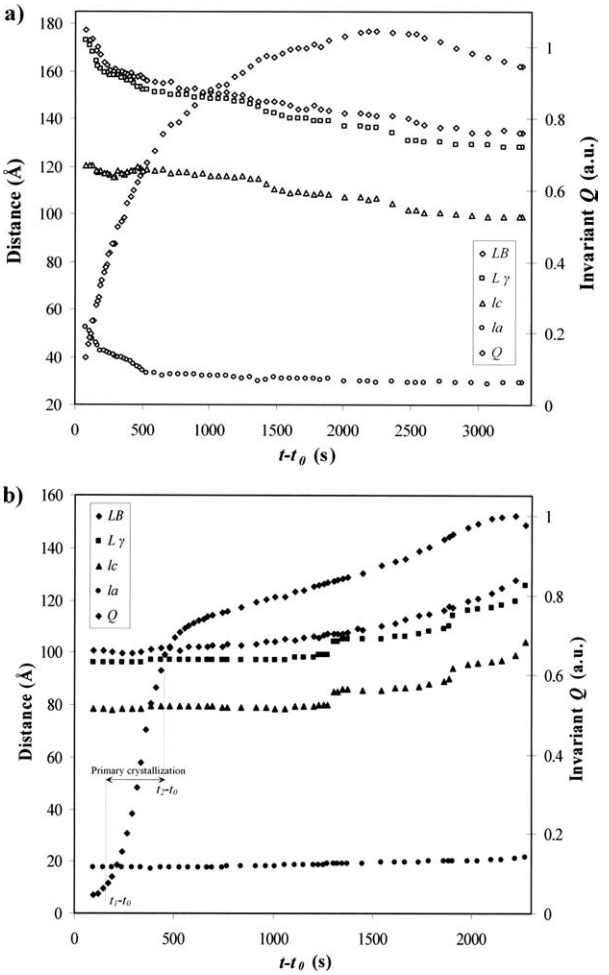

Figure 9 Time evolution of the Bragg spacing, L_B, long period from correlation function, $L_{\ddot{y}\ \ddot{I}}$, crystal thickness, l_c, amorphous thickness, l_a, and scattering invariant, Q, during nonisothermal hot (a) and cold (b) crystallization performed at 3°C/min with PGL-P(GL-*co*-TMC)-PGL samples.

the centers of gravity of two adjacent crystals appears to be higher than twice the most probable distance between the centers of gravity of a crystal and its adjacent amorphous layer. This suggests a broader distribution of the layer widths of the major component, which in this case corresponds to the crystal phase. Differences were more significative for the cold crystallized samples (9.7 nm respect 7.6 nm) before the melt-recrystallization process took place.

Data obtained during a nonisothermal hot crystallization reveal a decrease in both L_B and L_γ long spacings at the beginning of the process (i.e., during primary crystallization), as shown in Figure 9(a). These changes are basically due to the decrease on the amorphous layer thickness, which suggests an improved arrangement of folding surfaces. Furthermore, it is also possible to determine that crystalline lamellar thickness decreases significantly throughout the crystallization process, which means that a lamellar insertion mechanism occurs (i.e., formation of thinner lamellar crystals between loosely stacked primary lamellae). This insertion is more important when the cooling rate is slower and explains the differences between morphological parameters found when the cooling rate was varied [Fig. 7(c)]. Note that crystallization takes place at lower temperatures when the cooling rate is increased. Consequently, a lower crystalline lamellar thickness should be expected if the insertion mechanism were not relevant. It is also interesting that the long period at the beginning of crystallization varies, as expected from the change in the crystallization temperature, from 17.3 to 16.0 nm when the cooling rate changes from 3 to 20°C/min, respectively.

Figure 9(a) also shows the time evolution of the scattering invariant during nonisothermal crystallizations at a cooling rate of 3°C/min which reveals a typical behavior where invariant Q increases with time. However, it is interesting to note that at temperatures lower than 70°C (i.e. more than 2500 s) the invariant starts to decrease probably as a consequence of an increase on the electronic density of the inerlamellar amorphous phase.

The morphological parameters remain practically constant throughout the cold crystallization process [Fig. 9(b)], suggesting that, in this case, the insertion mechanism is not significant. However, a remarkable increase in both the long period and crystalline lamellar thickness is observed at high temperatures (long crystallization time) where melting and recrystallization of the initial lamellae occur. In this way, crystalline lamellar thickness increases from 9.7 nm to 12.0 nm during this recrystallization process. Note that the final thickness is similar to that obtained during the hot nonisothermal crystallization (12.9 nm). The evolution of the Q invariant during the cold crystallization experiment shows a sigmoidal increase with time where could be well distinguished: (a) the induction time, t_1, at which the SAXS profile starts to show a peak; (b) the zone associated to primary crystallization where the intensity of the SAXS peak continuously increases at a rapid rate; and (c) the time at which secondary crystallization starts, t_2. The SAXS invariant curve shows also a posterior increase with time which can mainly be attributed to the decrease of the electronic density of the interlamellar amorphous phase as above explained, or indeed to the hot crystallization process that occurs just before fusion.

The evolution of crystallinity during nonisothermal hot crystallizations was estimated from WAXD profiles [Fig. 5(b)]. Thus, the integrated intensity for each crystal reflection and the amorphous backgrounds were measured for the time-resolved spectra. Pearson VII fuctions were used to fit the amorphous backgrounds and all crystal reflection peaks. By dividing the total intensities of the crystalline reflections I_c by the overall intensity I_T, a measure of

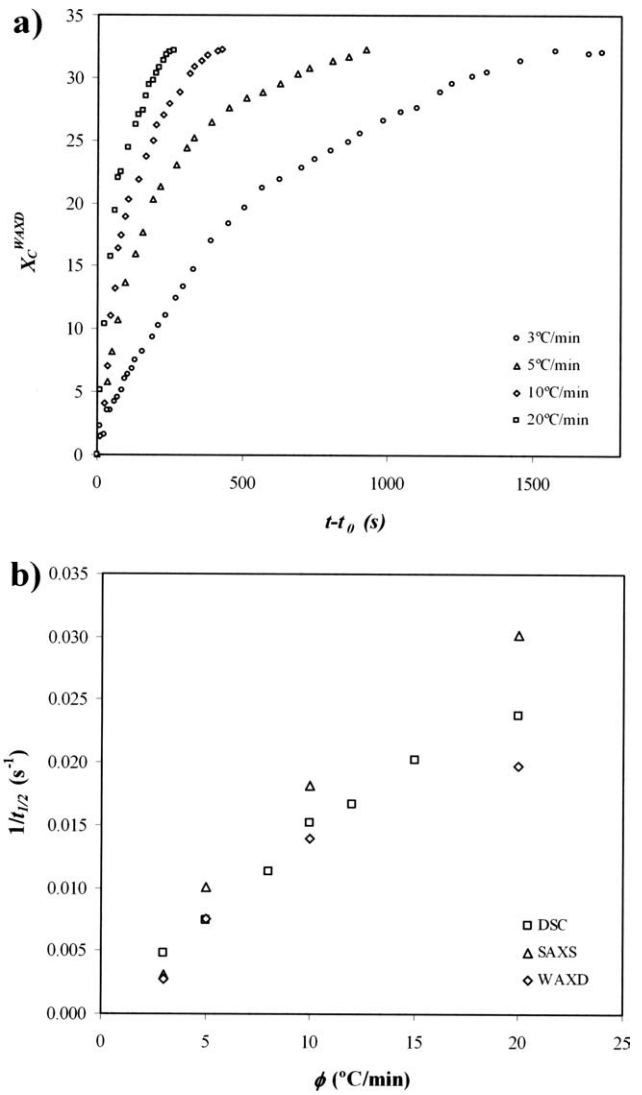

Figure 10 a) Time evolution of WAXD crystallinity during nonisothermal hot crystallization performed at the indicated cooling rates. (b) Comparison between the reciprocal of the half crystallization time determined by DSC, SAXS and WAXD for nonisothermal hot crystallization of PGL-P(GL-*co*-TMC)-PGL.

the mass fraction of the crystalline phase in the sample, X_c^{WAXD}, was obtained. The time evolution of WAXD crystallinity is displayed in Figure 10(a) for representative hot crystallizations. Crystallinity profiles are very similar to those of the SAXS invariant (obviously in the temperature range where crystallization takes place) and the relative degree of crystallinity evaluated by DSC. This agreement is better shown by considering the values of the half crystallization time ($\tau_{1/2}$), as listed in Figure 10(b) for the hot crystallization process. Larger discrepancies between DSC WAXD and SAXS data were observed at the highest cooling rate due to the shorter time involved and the higher relative error associated with the measure.

WAXD measurements indicate that relative crystallinities could be obtained in the 32–34% range at the end of the hot crystallization process regardless of the cooling rate. This crystallinity decreased slightly in the cold nonisothermal crystallization . ($\sim$ 31%). It is remarkable that the melt-recrystallization process occurring just before fusion did not result in a significant increase in the final crystallinity of the sample (e.g., a change from 31–33% was observed for a heating run of 3°C/min). This observation is in agreement with previous DSC calorimetric studies[11] where no exothermic peaks before fusion were detected in the heating runs of melt quenched samples.

Combined SAXS and WAXD data were also used to verify the assignment of l_a and l_c thicknesses, which could not be distinguished from the analysis of the correlation function.[32–35] Thus, the ratio between X_c^{WAXD} and X_c^{SAXS} [determined as $l_c/(l_c + l_a)$] is an estimate of the volume-filling fraction of the lamellar stacks, X_S, which should be lower than 1 for a correct assignment. For example, ratios of 0.40 and 0.78 were determined at the end of crystallization for cold and hot crystallized samples at a rate of 3°C/min, respectively. It seems that amorphous phase domains exist between the lamellar stacks and that they are less significant in the hot crystallized samples.

CONCLUSIONS

Nonisothermal optical microscopy analysis was successful to measure the spherulitic growth rate of PGL-P(GL-*co*-TMC)-PGL over a wide temperature interval. Data obtained from both cold and hot crystallization experiments were consistent and allowed to fully determine the bell shaped curve that defines the dependence between the crystal growth rate and the temperature. The maximum crystallization rate was found to occur at a temperature of 125°C. The typical Lauritzen and Hoffman analysis showed a single crystallization regime with parameters $U^* =$ 1575 cal/mol; $T_\infty = T_g - 30$ K and $K_g = 2.45\ 10^5$ K^2 that were in agreement with previous data derived from isothermal experiments.

The isoconversional approach proposed by Vyazovkyn and Sbirrazzuoli has been revealed highly effective to estimate crystallization parameters from cold and hot nonisothermal crystallization data obtained by DSC experiments. In this way, the maximum rate was found at a temperature of 127°C and a single regime with parameters $U^* = 1675$ cal/mol; $T_\infty = T_g -$ 30 K and $K_g = 2.30\ 10^5$ K^2 was determined. The close agreement between calorimetric and optical microscopy analyses suggests a linear dependence between the overall and the crystal growth rates of PGL-P(GL-*co*-TMC)-PGL, as it was previously deduced from isothermal crystallization studies.

Significant differences in lamellar morphology were found between hot and cold crystallized samples. Crystalline lamellar thickness was clearly lower in the latter case and remained practically insensitive to the crystallization time and the heating rate. In contrast, a lamellar insertion mechanism was deduced for melt-crystallized samples. Cold crystallized samples experimented a reorganization process just at some degrees before fusion which conduced to a significant increase of the crystal lamellar thickness.

The authors thank Dr. François Fauth and Dr. Ana Labrador of the CRG BM16 beamline staff of CELLS (Consortium for the Exploitation of the Synchrotron Light Laboratory). They also thank B. Braun Surgical S. A. for the collaboration and support.

References

1. Frazza, E. J.; Schmitt, E. E. J Biomed Mat Res Symp 1971, 1, 43.
2. Chu, C. C. Wound Closure Materials and Devices; CRC: Boca Raton, 1997; pp 65–106.
3. Middleton, J. C.; Tipton, A. J. Med Plast Biomater Mag 1998, 3, 30.
4. Middleton, J. C.; Tipton, A. J. Biomaterials 2000, 21, 2335.
5. Wang, Z. G.; Hsiao, B. S.; Zong, X.; Yeh, F.; Zhou, J. J.; Dormier, E.; Jamiolkowski, D. D. Polymer 2000, 41, 621.
6. Hurrel, S.; Cameron, R. E. Biomaterials 2002, 23, 2401.
7. Fu, B. X.; Hsiao, B. S.; Chen, G.; Zhou, J.; Lin, S.; Yuan, J.; Koyfman, I.; Jamiolkowsky, D. D.; Dormier, E. Chin J Polym Sci 2003, 21, 159.
8. Nair, L. S.; Laurencin, C. T. Progr Polym Sci 2007, 32, 762.
9. Bezwada, R. S.; Jamiolkowski, D. D.; Lee, I. Y.; Agarwal, V.; Persivale, J.; Trenka-Bethin, S.; Erneta, M.; Persivale, J.; Suryadevara, J.; Yang, A.; Liu, S. Biomaterials 1995, 16, 1141.
10. Noorsal, K.; Mantle , M. D.; Gladden, L. F.; Cameron, R. E. J Appl Polym Sci 2005, 95, 475.
11. Díaz-Celorio, E.; Franco, L.; Puiggalí, J. J Appl Polym Sci 2010, 116, 577.
12. Rueda, D. R.; García-Gutiérrez, M. C.; Nogales, A.; Capitán, M. J.; Ezquerra, T. A.; Labrador, A.; Fraga, E.; Beltrán, D.; Juanhuix, J.; Herranz, J. F.; Bordas, J. Rev Sci Instrum 2006, 77, 033904.
13. http://www.ccp13.ac.uk/software/program/corfunc/corfunc.htm.
14. Chen, M.; Chung, C. T. J Polym Sci Part B: Polym Phys 1998, 36, 2393.
15. di Lorenzo, M. L.; Cimmino, S.; Silvestre, C. Macromolecules 2000, 33, 3828.
16. di Lorenzo, M. L. Polymer 2001, 42, 9441.
17. Lauritzen, J. I.; Hoffman, J. D. J Appl Phys 1973, 44, 4340.
18. Suzuki, T.; Kovacs, A. J. Polym J 1970, 1, 82.
19. Vyazovkyn, S.; Sbirrazzuoli, N. Macromol Rapid Commun 2004, 25, 733.
20. Vyazovkin, S.; Dranca, I. Macromol Chem Phys 2006, 207, 20.
21. Vyazovkin, S.; Stone, J.; Sbirrazzuoli, N. J Therm Anal Calorim 2005, 80, 177.
22. Achilias, D. S.; Papageorgiou, G. Z.; Karayannidis, G. R. Macromol Chem Phys 2005, 206, 1511.
23. Cai, J. L.; Li, T.; Han, Y.; Zhuang, Y. Q.; Zhang, X. Q. J Appl Polym Sci 2006, 100, 1479.
24. Botines, E.; Puiggalí, J. Eur Polym J 2006, 42, 1595.
25. Gestí, S.; Zanetti, M.; Lazzari, M.; Franco, L.; Puiggalí, J. J Polym Sci Part B: Polym Phys 2008, 46, 2234.
26. Martínez-Palau, M.; Franco, L.; Puiggalí, J. J Polym Sci Part B: Polym Phys 2008, 46, 121.
27. Friedman, H. J Polym Sci Part C: Polym Symp 1964, 6, 183.
28. Chatani, Y.; Suehiro, K.; Okita, Y.; Tadokoro, H.; Chujo, K. Makromol Chem 1968, 113, 215.
29. Furuhashi, Y.; Iwata, T.; Sikorski, P.; Atkins, E. D. T.; Doi, Y. Macromolecules 2000, 33, 9423.
30. Vonk, C. G.; Kortleve, G. Kolloid Z Z Polym 1967, 220, 19.
31. Vonk, C. G. J Appl Cryst 1975, 8, 340.
32. Hsiao, B. S.; Gardner, K. H.; Wu, D. Q.; Chu, B. Polymer 1993, 34, 3986.
33. Ikada, Y.; Jamshida, K.; Tsuji, H.; Hyoan, S. H. Macromolecules 1987, 20, 906.
34. Kruger, K. N.; Zachmann, H. G. Macromolecules 1993, 26, 5202.
35. Hsiao, B. S.; Wang, Z.; Yeh, F.; Yan, G.; Sheth, K. C. Polymer 1999, 40, 3515.